Simulating the IHOP_2002 Fair-Weather CBL with the WRF-ARW–Noah Modeling System. Part II: Structures from a Few Kilometers to 100 km across

MARGARET A. LEMONE, FEI CHEN, MUKUL TEWARI, AND JIMY DUDHIA

National Center for Atmospheric Research, Boulder, Colorado*

BART GEERTS AND QUN MIAO

Department of Atmospheric Sciences, University of Wyoming, Laramie, Wyoming

RICHARD L. COULTER

Argonne National Laboratory, Chicago, Illinois

ROBERT L. GROSSMAN

Colorado Research Associates, Boulder, Colorado

(Manuscript received 13 March 2009, in final form 24 September 2009)

ABSTRACT

Fair-weather data along the May–June 2002 International H_2O Project (IHOP_2002) eastern track and the nearby Argonne Boundary Layer Experiments (ABLE) facility in southeast Kansas are compared to numerical simulations to gain insight into how the surface influences convective boundary layer (CBL) structure, and to evaluate the success of the modeling system in replicating the observed behavior. Simulations are conducted for 4 days, using the Advanced Research version of the Weather Research and Forecasting (WRF) model coupled to the Noah land surface model (LSM), initialized using the High-Resolution Land Data Assimilation System (HRLDAS). Because the observations focus on phenomena less than 60 km in scale, the model is run with 1-km grid spacing, offering a critical look at high-resolution model behavior in an environment uncomplicated by precipitation.

The model replicates the type of CBL structure on scales from a few kilometers to ~100 km, but some features at the kilometer scales depend on the grid spacing. Mesoscale (tens of kilometers) circulations were clearly evident on 2 of the 4 days (30 May and 20 June), clearly not evident on 1 day (22 June), with the situation for the fourth day (17 June) ambiguous. Both observed and modeled surface-heterogeneity-generated mesoscale circulations are evident for 30 May. On the other hand, 20 June satellite images show north-northwest–south-southeast cloud streets (rolls) modulated longitudinally, presumably by tropospheric gravity waves oriented normal to the roll axis, creating northeast–southwest ridges and valleys spaced 50–100 km apart. Modeled cloud streets showed similar longitudinal modulation, with the associated two-dimensional structure having maximum amplitude above the CBL and no relationship to the CBL temperature distribution; although there were patches of mesoscale vertical velocity correlated with CBL temperature. On 22 June, convective rolls were the dominant structure in both model and observations.

For the 3 days for which satellite images show cloud streets, WRF produces rolls with the right orientation and wavelength, which grows with CBL depth. Modeled roll structures appeared for the range of CBL depth to Obukhov length ratios ($-z_i/L$) associated with rolls. However, sensitivity tests show that the roll wavelength is also related to the grid spacing, and the modeled convection becomes more cellular with smaller grid spacing.

* The National Center for Atmospheric Research is sponsored by the National Science Foundation.

Corresponding author address: Margaret A. LeMone, NCAR Foothills Laboratory, 3450 Mitchell Lane, Boulder, CO 80301.
E-mail: lemone@ucar.edu

DOI: 10.1175/2009MWR3004.1

© 2010 American Meteorological Society

1. Introduction

This paper is the second of a two-part series that uses a combination of numerical simulations and observations to explore the relationship of surface heterogeneity and associated fluxes (W m^{-2}) of sensible heat H and latent heat (LE), to potential temperature Θ (K), mixing ratio Q (g kg^{-1}), depth, and convective structure on scales from 1 to 100 km in the fair-weather convective boundary layer (CBL), while evaluating the numerical simulations. The numerical simulations use the Advanced Research Weather Research and Forecasting (ARW-WRF) model (Skamarock et al. 2005), coupled to the Noah land surface model (LSM), which was initialized using the National Center for Atmospheric Research (NCAR) High-Resolution Land Data Assimilation System (HRLDAS; Chen et al. 2007). The data were collected in southeast Kansas using aircraft, surface flux towers, and three radar wind profilers, during May–June, 2002, as part of the International H_2O Project (IHOP_2002; Weckwerth et al. 2004, LeMone et al. 2007). The goal of IHOP_2002 was to improve prediction of convective precipitation in numerical weather prediction (NWP) models by improving the measurement and use of water vapor data, and by improving representation of the evolution of water vapor in numerical weather prediction models. Surface processes were emphasized because of their importance in the initiation and evolution of precipitating convection.

In LeMone et al. (2010, hereafter Part I), we focused on comparisons of observed and simulated surface fluxes, CBL thermodynamics, and CBL depth, and found that

- The Noah LSM produced an east–west gradient in H and LE consistent with the modeled soil moisture pattern, but not the observed variation associated with land cover, due to shortcomings in the input land-use and land-cover table.
- While modeled mean LE values and horizontal variation in the CBL depth compared reasonably well with observations, H and CBL depth were too high. This is likely due to too low a value of the coefficient C in Zilitinkevich's formulation used in relating the roughness lengths for heat and momentum in the Noah LSM, with too-low simulated soil moisture playing a secondary role.

Here, we evaluate the ARW-WRF–Noah modeling system's ability to simulate convective circulations in the fair-weather CBL on scales from a few kilometers to ~100 km. The region (the vicinity of the triangle and "eastern track" in Fig. 1) is characterized by a mix of mostly grassland (green) and winter wheat (senescent, harvested by mid-June), with trees bordering many fields and waterways. The track extends across the eastern side of the Walnut River watershed southeast of Wichita, Kansas, and into the watershed to the east.

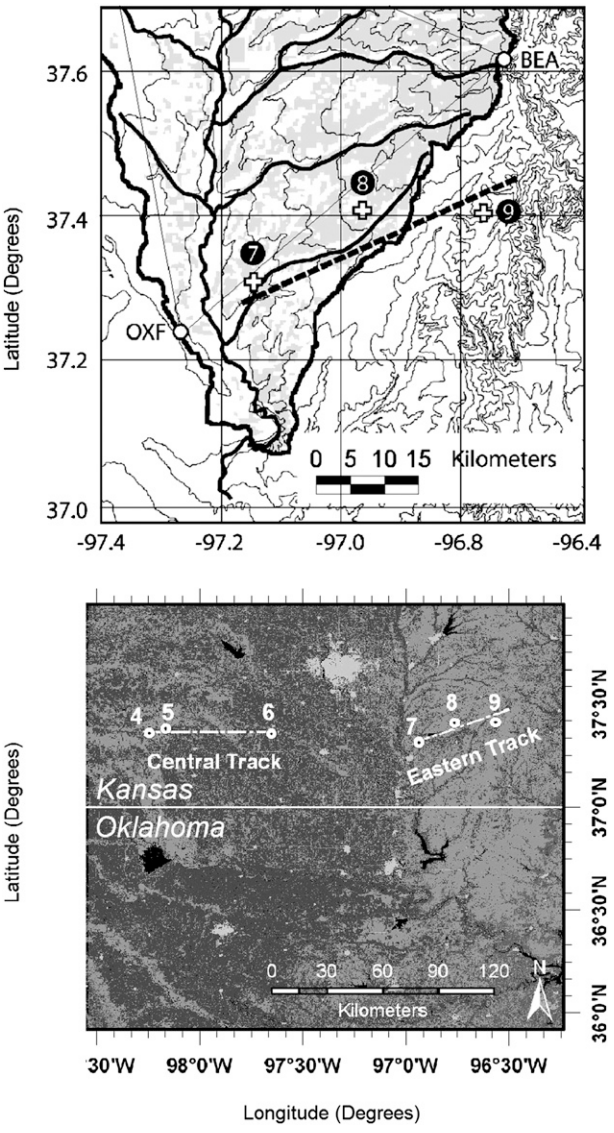

FIG. 1. Eastern track, instrumentation, and land use. (top) Instrumentation superimposed on terrain contours (interval = 20 m) in the Walnut River watershed in southeast Kansas. Thick lines: outline of watershed, the Walnut River, and its tributaries; within the watershed, shading = grassland; no shading = mostly cropland. Thick dashed line: eastern flight track. Partial triangle (fine solid lines) connects the three ABLE radar wind profilers at Oxford (OXF; 37.27°N, 97.10°W); Beaumont (BEA; 37.63°N, 96.54°W), and Whitewater (not shown, but on the NW vertex of the triangle at 37.84°N, 96.19°W or 63 km NNW (azimuth 350°) of OXF. (bottom) Central and eastern tracks (dot–dash lines), superimposed on land use/land cover: light gray = grasslands; dark gray = cropland; white = urban; black = open water. Numbers and symbols in both frames correspond to surface flux sites.

The effects of surface heterogeneity on fair-weather CBL structure have been the subject of numerous

TABLE 1. Boundary layer King Air flights and environmental conditions along the eastern track (z_i = CBL depth).

Date	No. of legs low (avg height range, m AGL)	No. of legs middle (avg height range, m AGL)	No. of legs high (avg height range, m AGL)	Days after last rain*	Avg wind for "low" legs (direction/speed, (°/m s^{-1})	z_i 1830 UTC (m)	Clouds (airborne observers' notes, satellite images)
30 May 2002	8 (62–73)		6 (523–688)	3/5.5*	159/3.9	900	Ci; isolated small Cu; haze at BL top
17 Jun 2002	6 (60–79)	6 (135–271)	6 (574–743)	1.7	201/7.7	1240	Scattered Cu humulis in streets
20 Jun 2002	5 (62–66)	6 (151–408)	5 (545–765)	4.7	162/5.3	1250	Scattered Cu humulis in streets; Ci
22 Jun 2002	10 (58–67)		6 (752–897)	6.7	179/9.4	1260	Scattered Cu humulis in streets

* 30 May, 3 days after light (5–10 mm) rain on 27 May; 5.5 days after a 5–10-mm event; 5.5 days after 9–20 mm, 6 days after 18–85-mm rainfall; other significant event ended 0345 UTC 16 Jun 2002, which deposited around 25 mm of rain over about a 5-h period.

modeling studies, some of which incorporate observational data, and a few observational studies. Mesoscale models have been applied to demonstrate the potential importance of CBL mesoscale circulations (~10–100 km) generated by surface heterogeneity and to understand the scales favored for such circulations (e.g., Chen and Avissar 1994; Baidya Roy and Avissar 2000; Baidya Roy et al. 2003). Reen et al. (2006) and Desai et al. (2006) combined observations and a mesoscale model to look at the effects of heterogeneous surfaces on CBL structure in real situations. Larger and faster computers have enabled numerous large-eddy simulations (LESs) to study the structure and evolution of mesoscale CBL circulations (e.g., Avissar and Schmidt 1998; Letzel and Raasch 2003; Patton et al. 2005; Kang and Davis 2008). However, observational documentation of mesoscale circulations is typically sketchy (e.g., Mahrt et al. 1994; LeMone et al. 2002; Kang et al. 2007; Taylor et al. 2007), with the significant exception of circulations along the dryline that lead to precipitating convection (Ogura and Chen 1977 and many subsequent papers, recognizing that factors other than surface heterogeneity are also important for the dryline). More traditional LESs have examined CBL-depth scale (~few kilometers, hereafter referred to as kilometer scale) structure for decades (e.g., Deardorff 1972; Moeng and Sullivan 1994), and there has been limited attention to kilometer-scale structure generated in high-resolution mesoscale model simulations (Trier et al. 2004; Miao and Chen 2008).

Our goal to compare CBL structure and evolution at the scales observed requires high-resolution runs. The choice of an LES to simulate real-world situations is appealing, since large CBL eddies are resolved. Indeed Conzemius and Fedorovich (2008) used LES to simulate of CBL development near the western track, and Gorska et al. (2008) used LES to simulate of mesoscale circulations along the eastern track. However, these studies were hindered by the need for periodic boundary conditions. Moreover, CBL structure can be influenced by interaction with tropospheric gravity waves (e.g., Clark et al. 1986; Balaji et al. 1993), requiring inclusion of a deeper domain than ordinarily used in LES. These factors, along with the convenience of having an NWP model with a reasonably robust surface model, led to the choice to run ARW-WRF run at 1-km resolution. We recognize the potential problems created by "double counting" associated with partially resolving CBL-scale motions and using a CBL scheme, but note the developing literature of high-resolution ARW-WRF runs that appear successful, even at very high resolution (e.g., Davis et al. 2008, Miao and Chen 2008). Furthermore, actual comparisons to data such as done here can help us understand the limitations of stretching ARW-WRF beyond its expected capabilities.

The paper is outlined as follows. Data collection and analysis are discussed in section 2, with model runs and analysis of results summarized in section 3. Section 4 compares the observed and modeled CBL structure from kilometer-scale to mesoscale (~10–100 km), drawing from some sensitivity runs to help interpret the model CBL convective structure. The results are summarized in section 5.

2. Data collection and analysis

The four fair-weather days examined had scattered clouds and wind from approximately south-southwest to southeast (Table 1). Winds at 65 m above ground level (AGL) vary from 3.9 m s^{-1} on 30 May to 9.4 m s^{-1} on 22 June. Timing of the most recent rainfall ranged from 1.7 to 6.7 days previous. Figure 1 shows a higher density of crops (mainly winter wheat) to the west and mainly grasslands to the east, relative to the eastern track and for at least 100 km to the south. The band of

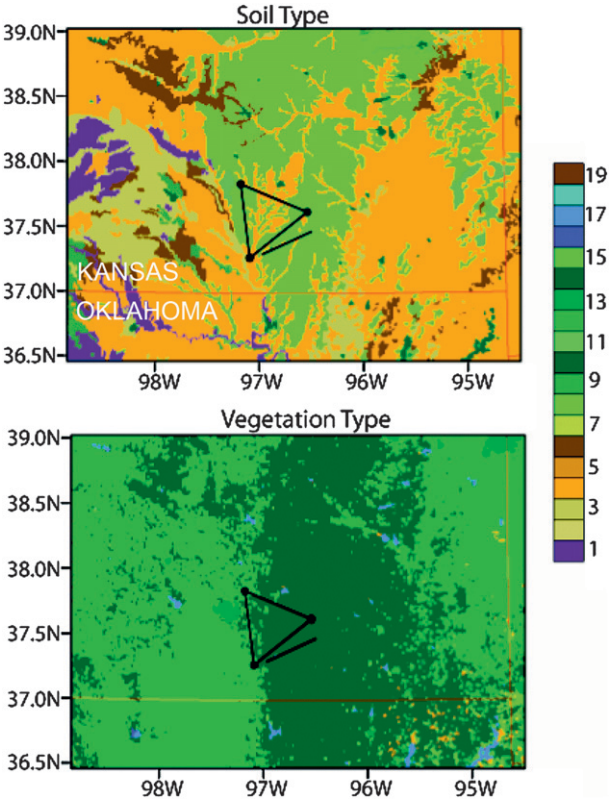

FIG. 2. (top) Soil type and (bottom) land use/land cover for inner domain (d03; Fig. 3) with state boundaries (red), profiler triangle, and eastern track (solid black lines) included. Soils near the eastern track: 8 = silty clay loam, 4 = silt loam; elsewhere in figure: 1 = sand, 2 = loamy sand, 3 = sandy loam, 6 = loam, 7 = sandy clay loam, 9 = clay loam, 10 = sandy clay, 11 = silty clay, 12 = clay, 13 = organic material, and 14 = water. For vegetation, near the eastern track: 10 = grasslands, 12 = croplands, 13 = urban, and 17 = water; other vegetation in figure: 4 = deciduous broadleaf forests and 16 = barren and sparsely vegetated.

winter wheat extends south to the Oklahoma–Kansas border; south of the border, the winter wheat band extends southwestward into Texas. The dominant soil type along the flight track is silty clay loam (Soil Survey Geographic Database; more information is available online at http://dbwww.essc.psu.edu/dbtop/doc/statsgo/statsgo_info.html; Fig. 2), consistent with the observed near-surface soil type at the IHOP_2002 surface sites.

As in Part I, aircraft data are from the University of Wyoming King Air, which flew straight and level legs along the ~46-km long eastern track (Fig. 1). While at least 5 passes were flown between 60 and 70 m AGL, there are data collected from at least 1 other altitude range (Table 1). Aircraft-relative winds were measured by a Rosemount 858AJ/1332 differential pressure gust-probe system. Aircraft position and motion relative to the ground were measured by a Honeywell Laseref SM inertial navigation system and corrected using GPS to within 100 m horizontally. Aircraft altitude was based on a King KRA5 radio altimeter for heights below 610 m; and an APN159 radar altimeter for heights above 610 m. Estimates of virtual potential temperature Θ_v are based on water vapor densities from a LiCor 6262 gas analyzer,[1] flight-level air temperatures from a reverse-flow platinum-resistance thermometer built at the University of Wyoming, and pressure from a Rosemount 1201 sensor. Data were made available at 25 Hz and as 1-s averages.

Statistics on flight-level wind and thermodynamics were based on the 1-s data. Aircraft-based divergences were computed from the along-track wind component using least squares best-fit lines to each flight track. Values at specific times could then be computed from a least squares best fit line to the divergence time series at each level.

To calculate the Obukhov length L, we use leg-averaged flux measurements from the King Air following Strassberg et al. (2008), and fluxes from the three towers along the eastern track, located on grassland sites at positions 7, 8, and 9 in Fig. 1. These measurements are described in detail in Part I and LeMone et al. (2007).

Argonne National Laboratory's Atmospheric Boundary Layer Experiments (ABLE; ABLE is no longer operating; however, the data are available at http://gonzalo.er.anl.gov/ABLE; Klazura et al. 2006) facility radar wind profilers were used to obtain CBL depth and convergence. The locations of the two profilers used for boundary layer (BL) depth—Beaumont and Oxford, Kansas—are shown in Fig. 1. The BL height was defined as the center height of the gate just below the maximum signal-to-noise dropoff rate with height (Coulter and Holdridge 1998). For convergence estimates, the ABLE Whitewater profiler was combined with those at Beaumont and Oxford. The Whitewater profiler lies ~63 km north-northwest of Oxford (~350° azimuth) so that the three profiles form a nearly equilateral triangle. The vertical resolution of the profiler data is of the order of 60 m. Radar wind profilers can in principle measure vertical wind directly, but in the CBL this measurement tends to be negatively biased (Angevine 1997).

3. ARW-WRF runs

The model runs are described in detail in Part I, so we provide only essential detail here. Our control runs use ARW-WRF version 2.1.2 with the Yonsei University

[1] There is a small bias (~1 g m^{-3}) between the LiCor, and the Lyman α, which was used in Part I because it was referenced to an EG and G chilled-mirror dewpointer. Since only horizontal changes in Θ_v are considered, the bias should not influence the results.

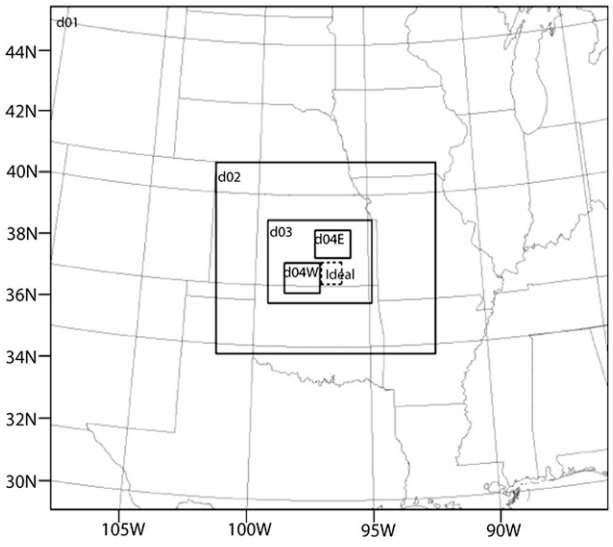

FIG. 3. Domains for ARW-WRF runs, with horizontal grid spacing. Outer domain (d01): 9 km; intermediate domain (d02): 3 km; inner domain (d03): 1 km. Innermost domains for sensitivity studies include the two 333-m grid spacing domains for 22 Jun (represented by solid rectangles d04E and d04W), and the rectangle used for the idealized runs using 20 Jun data (labeled "ideal"), which is dashed because (i) it varies in size according to grid spacing, and (ii) there are no outer domains for the idealized runs.

(YSU) PBL scheme (Hong et al. 2006), coupled to the Noah LSM (Chen and Dudhia 2001; Ek et al. 2003). The simulations, for the four fair-weather days in Table 1, start at 1200 UTC and run for 24 h, using the nested domains shown in Fig. 3. The vertical grid contains 30 full-sigma levels from the surface to 50 hPa, of which the lowest 8 levels are below 1 km AGL (lowest level 28 m AGL) in order to have finer resolution in the CBL. The horizontal grid spacing (number of points) of the three outer domains are 9 km (237 × 201), 3 km (280 × 229), and 1 km (391 × 289), respectively. Initial and boundary conditions are from the National Centers for Environmental Prediction (NCEP) 6-hourly Eta Data Assimilation System (EDAS) on a 40-km grid. In the control ARW-WRF simulation, the Noah LSM is initialized by volumetric soil moisture and temperature profiles and skin temperature obtained from HRLDAS (Chen et al. 2007), which is run offline but on the same nested WRF grid for an 18-month spinup period ending at the initialization time of each ARW-WRF simulation (here, runs start 1 January 2001). The input data at the surface are default values except for the land-use characteristics, which are based on Moderate resolution Imaging Spectroradiometer (MODIS) data from the Boston University Department of Geography (see online at http://www-modis.bu.edu/landcover/; Fig. 2).

We did several sensitivity runs to see whether the modeled CBL-scale convective structure was robust. Two runs tested the effects of horizontal resolution using data from 22 June; and several idealized runs were conducted using data from 20 June to assess the impact of grid spacing, surface properties, and filtering (Table 2). Two higher-resolution runs for 22 June were run using the same version of ARW-WRF (ARW-WRF V2.1.2) as the control runs, with a fourth domain with 333-m grid spacing (Fig. 3), with initial surface conditions interpolated from the 1-km HRLDAS results.

The idealized runs used the public-release ARW-WRF version 3 (ARW-WRF V3), with all points in the domain initially assigned surface characteristics and meteorological data for a typical point on the eastern track (37.4188°N, 96.6472°W), and in domains centered at this point (Fig. 3). Initial surface properties in the idealized runs were varied horizontally by randomly perturbing the initial volumetric soil moisture profile and/or T_s, using a uniform distribution with ranges of ±0.02 and ±0.01 K, respectively. We varied grid spacings for both the surface and atmosphere grid together and separately, ran simulations with and without the Knievel et al. (2007) filter to damp unresolved motions ($<6\Delta x$), and changed the domain depth for some runs. The grid points in the innermost domain varied from 226 × 226 for the 200-m runs to 101 × 101 for the remaining runs. Because input data were based on only one point, winds had to be determined using an option in ARW-WRF that maintains the geostrophic part with an implicit pressure gradient, with only the ageostrophic component responding to the Coriolis acceleration. Table 2 will be discussed in greater detail in section 4b.

A final sensitivity run was conducted to assess the effect of the Knievel filter on mesoscale structure. Using the same model setup as for the control runs, we ran ARW-WRF V3 for 30 May with and without the Knievel filter.

4. Results

a. *Horizontal variability in virtual potential temperature*

As noted in Part I, Θ increased westward along the eastern track in both model results and observations. The largest east–west difference was for 30 May, and the smallest for 22 June. These trends are consistent with the east–west differences in Θ_v, which extends through the CBL (Table 3). The differences between these two days are also consistent with the modeled soil moisture patterns, which show stronger contrast along the flight track on 30 May than for 22 June (Fig. 4).

To see whether these along-track Θ_v changes can result from horizontal heterogeneity alone (i.e., no synoptic-scale differential advection), we consider two idealized

TABLE 2. Effects of resolution on CBL structure. All idealized runs use ARW-WRF V3, with uniform vegetation (grassland) and soil texture (silty clay loam), and surface, subsurface, and meteorological data from 37.4188°N, 96.6472°W on 20 June, with initial T_s and/or volumetric soil moisture varied using random perturbations. 22 Jun runs use ARW-WRF V2.1.2. Y = "yes," N = "no," h_{WRF} = CBL depth from ARW-WRF, averaged over domain unless otherwise indicated. "Filt" refers to the Knievel et al. (2007) filter used in ARW-WRF to damp out unresolved motions; "Nest" refers to whether the finest resolution was a result of nesting.

Run	Noah grid Spacing (km)	Atmospheric grid spacing (km)	Domain top (km)	Filt	Nest	Roll spacing (*x* direction) 1800 UTC (km)	h_{WRF} 1800 UTC (km)	λ_{roll}/h_{WRF}* 1800 UTC	h_{WRF} 2100 UTC (km)	Remarks
20 Jun idealized runs with surface skin temperature perturbations										
T1mix1_0.2NFs	1	0.2	5	N	Y	—	—	—	—	Cells
T1NF	1	1	20	N	N	n/a	1.14	n/a	1.68	Weak cellular 1800 UTC, weakly defined rolls 2100 UTC
T1	1	1	20	Y	N	n/a	1.14	n/a	1.68	No CBL convective structures
T2	2	2	20	Y	N	n/a	1.14	n/a	1.68	No CBL convective structures
T4	4	4	20	Y	N	n/a	1.14	n/a	1.68	No CBL convective structures
T10	10	10	20	Y	N	n/a	1.14	n/a	1.68	No CBL convective structures
20 Jun idealized runs with surface skin temperature and volumetric soil moisture perturbations										
TS5	5	5	20	Y	N	n/a	1.17	n/a	1.67	Irregular, 50-km roll-like structure at CBL top, 1800–2100 UTC
TS1	1	1	20	Y	N	6.7	1.16	5.1	1.68	Rolls, 6.7 km at 2100 UTC
TS1NF	1	1	20	N	N	4.0	1.16	3.1	1.66	Rolls, 4.8 km 2100 UTC
TS0.5	0.5	0.5	20	Y	N	3.5	1.20	2.6	1.69	Rolls, ~4 km 2100 UTC
TS0.5s	0.5	0.5	5	Y	N	3.9	1.26	2.8	1.67	Rolls, 4.6 km 2100 UTC
TS0.5NFs	0.5	0.5	5	N	N	2.4	1.17	1.8	1.67	Cellular conv. by 2100 UTC
TSmix1_0.5s	1	0.5	5	Y	N	3.1	1.17	2.4	1.67	Rolls, ~4 km at 2100 UTC
TSmix1_0.33NFs	1	0.333	5	N	Y	1.8	1.17	1.4	1.67	Rolls, cells to north
TSmix1_0.2NFs	1	0.2	5	N	Y	n/a	1.17	n/a	1.67	Rolls 1600 UTC but mostly cellular afterward
TSmix2_0.5sNF	2	0.5	5	N	Y	2.4	1.17	1.8	1.67	Rolls, larger at 2100 UTC
22 Jun, real data										
Control	1	1	20	N	Y	4.3	1.66	2.6		h_{WRF} for OXF, BEA, eastern track
HiResE	0.33	0.33	20	N	Y	2	—	—		Rolls and some cells
HiResW	0.33	0.33	20	N	Y	2	—	—		Rolls and some cells

* Roll aspect ratio, where λ_{roll} = roll spacing in *x* direction times cosine of roll orientation with respect to north.

TABLE 3. Observed parameters related to development of mesoscale circulations, interpolated to 1830 UTC unless otherwise indicated.

Date	70-m wind (Avg) ($m\ s^{-1}$)	z_i (leg center) (m)	$\langle\Theta_v\rangle$ (K)	$\overline{w\theta_{v,0,c}}$* ($K\ m\ s^{-1}$)	$\Delta\Theta_v = [\Theta_v(W) - \Theta_v(E)]$ at 70 m (Avg) (K)	$\Delta\Theta_v$ rest of BL (Avg) (K)	$D_{\Delta\Theta_v}$ (3) (km)	$t_{\Delta u_i}/D_{\Delta u_i}$ (5) (h)/(km)
30 May 2002	3.9	900	305.0	0.11	0.7	0.6	86	1.4/19
17 Jun 2002	7.7	1240	303.6	0.13	0.4	0.4	122	1.6/44
20 Jun 2002	5.3	~1250	306.7	0.10	0.3	0.3	83	2.1/40
22 Jun 2002	9.4	1260	306.6	0.11	0.2	0.2	90	3.1/107

* The subscript "*c*" represents the value at cool eastern end of the track at 1830 UTC calculated so that the average of the "warm" and "cool" values equal the leg averages.

trajectories that start out with the same Θ_v, one headed northward toward the western end of the flight track over dormant winter wheat and dry soils, and the second headed northward toward the eastern end over green grasses and wet soils, consistent with southerly winds passing over the vegetation and soil moisture depicted in Figs. 1 and 4. For simplicity, we assume that the surface virtual temperature fluxes $\overline{w\theta_{v,0}}$ along the trajectories are related such that $\overline{w\theta_{v,0,w}} = (1 + f)\overline{w\theta_{v,0,c}}$, where f is a positive constant, the subscript w denotes the warm western trajectory, and the subscript c denotes the cool eastern trajectory.

We assume[2] that $\overline{w\theta_{v,zi}}$, the virtual potential temperature flux at CBL top, is related to the surface flux via $\overline{w\theta_{v,zi}} \approx -0.2\overline{w\theta_{v,0}}$. Neglecting direct warming by radiative effects, the along-trajectory time rate of change of the virtual potential temperature averaged over z_i, $\langle\Theta_v\rangle$, is given by

$$\frac{d\langle\Theta_v\rangle}{dt} \approx \frac{1.2\overline{w\theta_{v,0}}}{z_i}. \quad (1)$$

Assuming the same z_i for both trajectories, and taking the difference between $d\langle\Theta_v\rangle/dt$ for air along the "warm" and "cool" trajectories:

$$\frac{d(\langle\Theta_v\rangle_w - \langle\Theta_v\rangle_c)}{dt} \approx \frac{\Delta(\Delta\langle\Theta_v\rangle)}{\Delta t_{\Delta\Theta_v}} \approx \frac{1.2f\overline{w\theta_{v,0,c}}}{z_i}. \quad (2)$$

Integrating (2) and recalling that $\Delta\langle\Theta_v\rangle$ is initially zero (trajectories start at the same $\langle\Theta_v\rangle$), we obtain the along-trajectory distance $D_{\Delta\Theta_v}$ required to develop a horizontal temperature difference $\langle\Delta\Theta_v\rangle$:

$$D_{\Delta\Theta_v} = St_{\Delta\Theta_v} \approx S\frac{\Delta\langle\Theta_v\rangle z_i}{1.2f\overline{w\theta_{v,0,c}}}, \quad (3)$$

where S is the wind speed along the trajectory. During the morning hours, $\overline{w\theta_{v,0,c}}$ and z_i change together (cf. Figs. 7 and 8 in Part I), keeping their ratio in (1)–(3) roughly constant. This enables us to use noontime values for crude estimates of $t_{\Delta\Theta_v}$ and $D_{\Delta\Theta_v}$.

Setting $f = 0.2$ and applying (3) to the four IHOP_2002 days, with S, $\Delta\langle\Theta_v\rangle$, z_i, and $\overline{w\theta_{v,0,c}}$ from Table 3, we find that $D_{\Delta\Theta_v}$ ranges from 83 to 122 km. From Figs. 1 and 2, observed and modeled upstream vegetation has gradients over these scales. The modeled horizontal gradient in soil moisture for 30 May (Fig. 4) and 17 June (not shown) are of sufficient scale; the soil moisture patterns of 20 (not shown) and 22 June (Fig. 4) are more irregular, but still exhibit a broad westward drying. A definitive calculation would have to account for fluxes, BL depths, and land cover along the actual trajectories. Having a deeper BL for the western trajectory would dilute the heating, and thus lengthen the time/distance required to produce a given $\Delta\langle\Theta_v\rangle$. Moreover, since terrain in the Kansas–Oklahoma region rises toward the west, constant surface air temperatures would mean that east–west convergence could increase the Θ gradient, with upslope easterlies to the east lowering Θ and downslope westerlies to the west raising Θ.

b. Convective-scale structure and clouds

On 3 of the 4 days, the ARW-WRF runs produced roll-type structures aligned with the CBL wind, with structure and orientation similar to that documented in satellite images (Fig. 5). From the figure, the model replicates the observed north–south cloud streets on 22 June, and south-southeast–north-northwest cloud streets that vary longitudinally on 20 June. For 17 June, ARW-WRF produces south-southwest–north-northeast linear roll structures with the same orientation of the cloud streets depicted in the satellite image. The radar composites in Fig. 6 suggest roll alignment corresponding to the cloud streets. The observed and modeled roll wavelength, about 4 km, is consistent with that associated with CBL rolls (~$3z_i$, e.g., LeMone 1973, land values from Fig. 4 in Young et al. 2002). However, this result could be

[2] Conzemius and Fedorovich (2006) suggest the relationship $\overline{w\theta_{v,zi}} \approx -0.2\overline{w\theta_{v,0}}$ applies if the shear at PBL top is small. Strassberg et al. (2008) found the shear to be small for the June days, and "small to moderate" for 30 May, with a z_i to surface flux ratio less than 0.2, so the relationship should apply reasonably well for the 4 days discussed here.

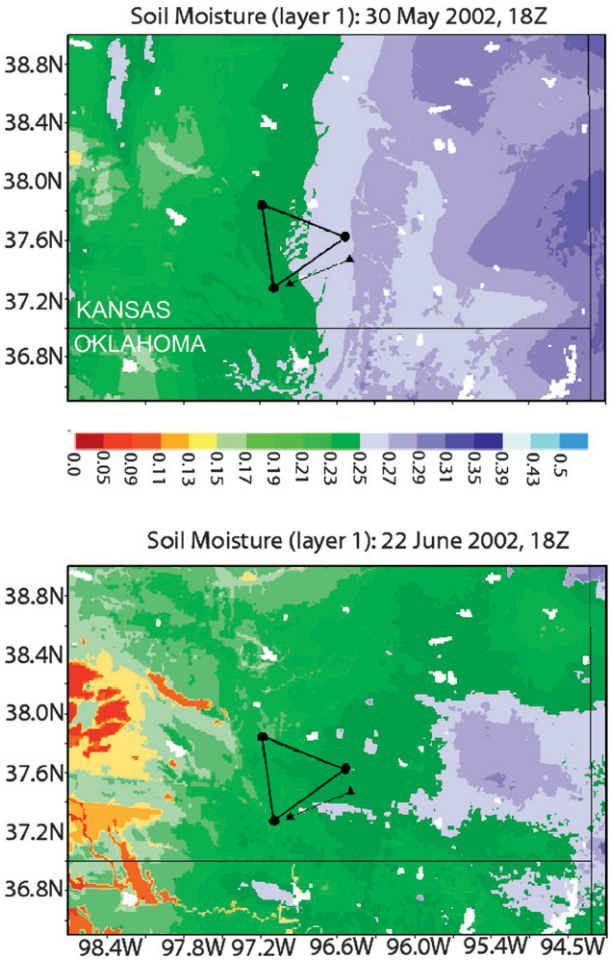

FIG. 4. Noah LSM volumetric soil moisture distribution for level 1(0–10 cm) in inner domain d03 (Fig. 3) for coupled run, at (top) 1800 UTC 30 May and (bottom) 1800 UTC 22 Jun 2002. White areas represent open water, thin black lines are state boundaries, and thick black lines represent the profiler triangle and eastern track.

fortuitous: for these 1-km grid simulations, 4 km is less than the ~6–10Δx quoted in Skamarock (2004) as the lower limit for properly resolving structure and amplitude.

The ARW-WRF did not produce clear-cut convective patterns on 30 May, with patches of irregular cellular convection and artificial-looking linear structures 2Δx wide near the flight track and profiler triangle (not well resolved in Fig. 5a). The Wichita Weather Surveillance Radar-1988 Doppler (WSR-88D) radar pattern in Fig. 6 also shows a cellular pattern. The 2Δx features probably result from the shallow CBL depth (Table 1), which reduces the expected convection scale (order CBL depth); and a combination of light winds (Table 1) and the numerical diffusion scheme in ARW-WRF version 2.1.2, which is less effective at reducing 2Δx features in light winds (Knievel et al. 2007).

The presence of CBL rolls (as opposed to cellular convection) corresponds to what occurs in nature. In Figs. 5 and 6, the rolls occur for values of $-z_i/L$ less than around 25, where L is the Obukhov length, as expected from previous work by Weckwerth et al. (1999) and others. Similarly, ARW-WRF simulations by Miao and Chen (2008) showed rolls for smaller $-z_i/L$ ratios and random convection for larger ratios, and Méso-NH (Lafore et al. 1998) simulations by Lothon et al. (2007) showed rolls transitioning to cells as $-z_i/L$ increased beyond 25.

For the observations, the "regional"[3] $-z_i/L$ ratios based on aircraft 46-km averages (Strassberg et al. 2008) seem to have a better correspondence to rolls than those based on the local flux tower data (Table 4). As shown by Strassberg et al. using data from 22 June, these regional values correspond to a momentum roughness length z_0 of 0.14 m, close to the value of $z_0 = 0.12$ prescribed for grassland in ARW-WRF. Note that the $-z_i/L$ threshold for roll occurrence is significantly exceeded for 20 June (Table 4) when we use u_* measured at the surface stations or use model fluxes with the local (0.02 cm) z_0 value; thus, additional evidence for the need to use regional values.

The good correspondence between modeled and observed type of convective structure was surprising, given the use of a PBL scheme designed for grid spacings much larger than 1 km (e.g., Wyngaard 2004) and the associated use of grid boxes with smaller width-to-height ratios (Wyngaard et al. 1998). To test the robustness of the convection type and scale in the ARW-WRF simulations, we ran a series of tests to assess the impact of surface perturbations and grid sizes on the characteristics of the CBL convection, summarized in Table 2. As seen from the table, the grid spacings for both the surface and the atmosphere were varied, sometimes separately.[4] Volumetric soil moisture (surface temperature T_s) was perturbed randomly using a uniform distribution with a range of ±0.02 (0.01 K) relative to the mean. On some runs, T_s was perturbed and soil moisture left constant. We also varied the depth of the model and horizontal diffusion (not shown). Each run is identified

[3] The "regional" fluxes, being based on momentum fluxes computed from fluctuations relative to a 46-km flight-leg linear trend, include the effects of trees, buildings, etc.; while the "local" fluxes, being based on surface flux sites that are in open areas, represent the surface sampled (in this case, grasses).

[4] The two grid sizes were always such that no interpolation was necessary. For example, for the larger grid 1 km, the smaller grid might be 500 m, so that the four 500-m squares exactly overlap with the 1-km squares. In this case, the 1-km grid square responds to the average of the values for the four 500-m squares; and the four 500-m squares respond to the 1-km square values.

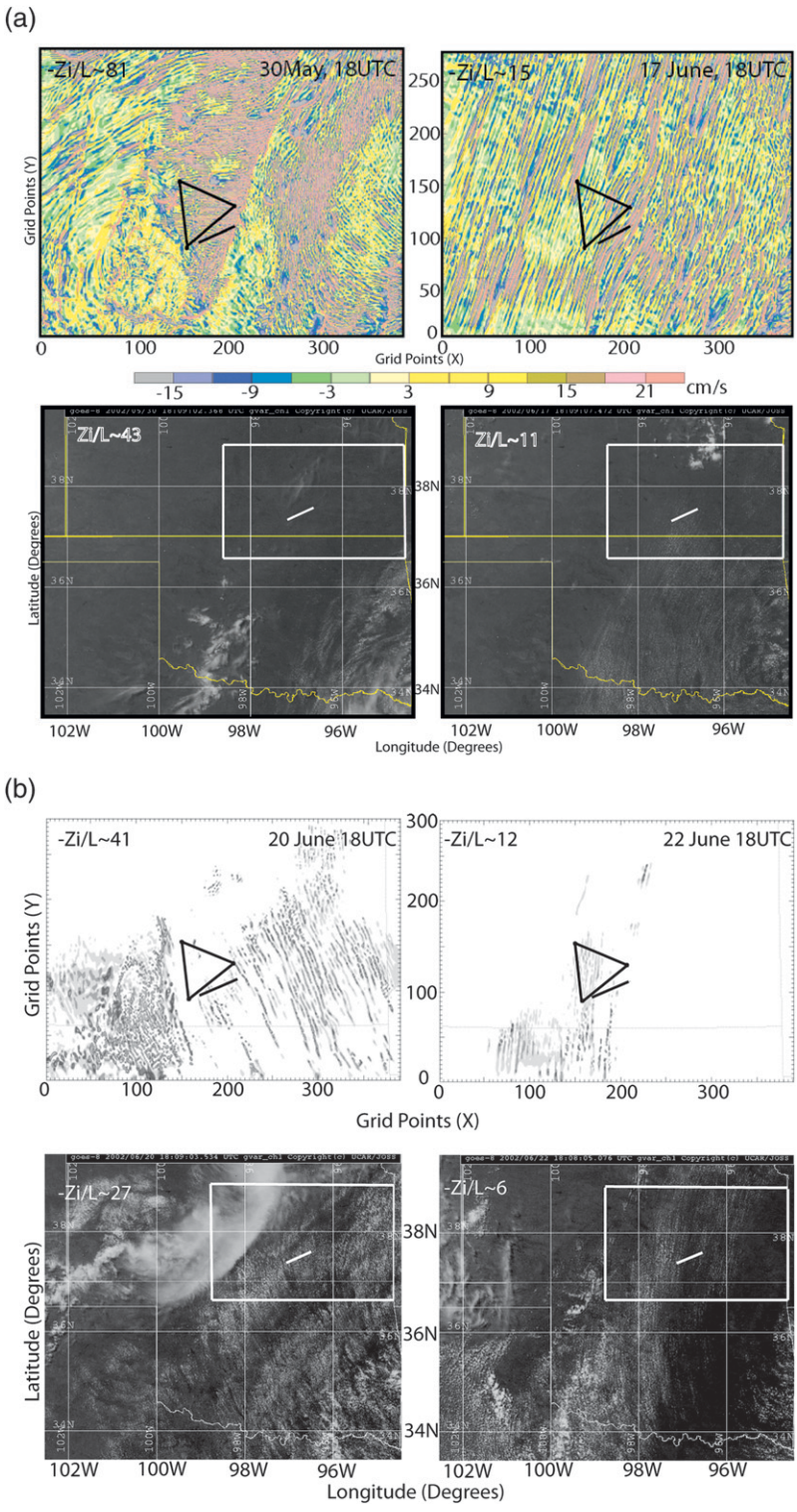

FIG. 5. (a) CBL convective patterns, as reflected by (top) mid-CBL (level 5, around 500 m) vertical velocity in ARW-WRF (1800 UTC) for domain d03 (1-km grid) and (bottom) cloud patterns in *GOES-8* (1809 UTC) image, for (left) 30 May and (right) 17 June. Model domain d03 and eastern track are included for scale and geographic reference. Values of $-z_i/L$ are for regional (grid scale) values of z_0 for observations (ARW-WRF) from Table 4. (b) As in (a), but for cloud fields (vertically integrated liquid water) on 20 and 22 June from *GOES-8* and ARW-WRF.

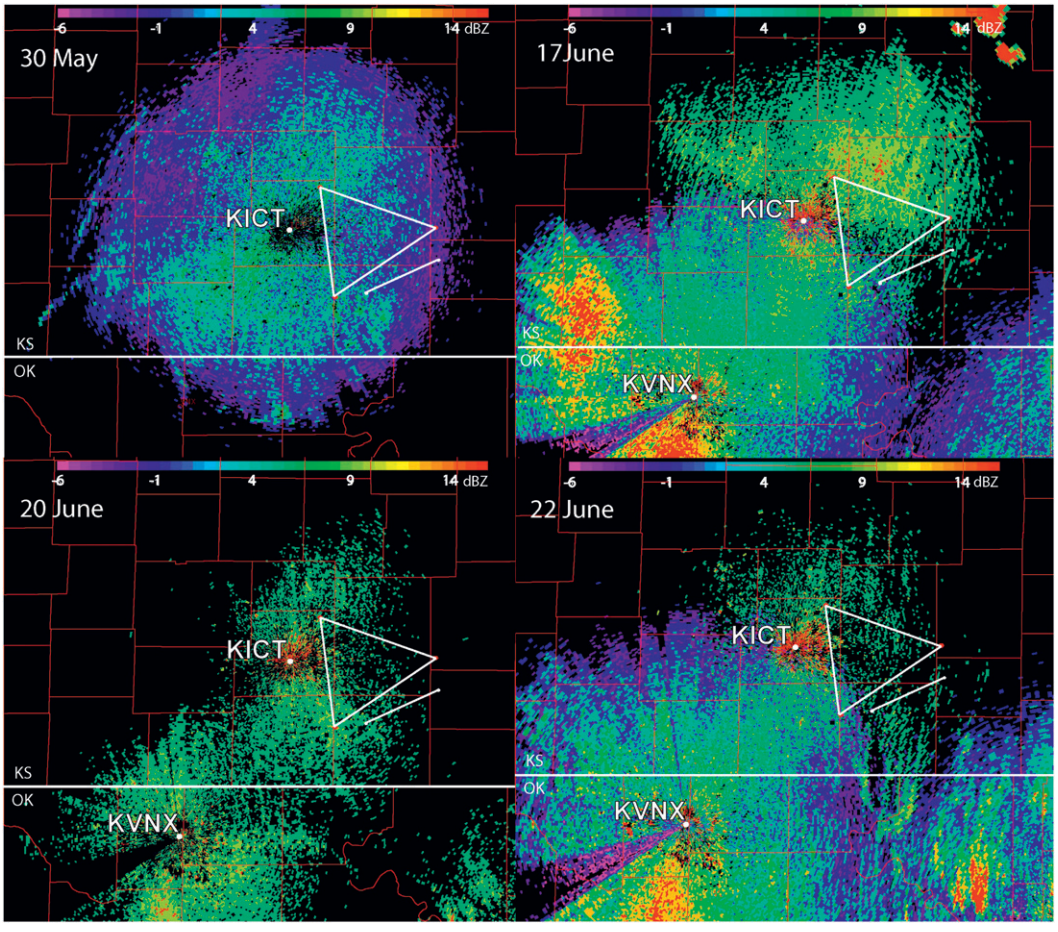

FIG. 6. CBL convective patterns at 1830 UTC revealed by clear-air return (dBZ) from the WSR-88D radars at Wichita, KS (KICT), Vance Air Force Base, OK (KVNX), and Tulsa, OK (bottom right in each frame, center off the figure). County lines, flight track and profiler triangle are included for reference. The stronger (weaker) returns are associated with clear-air mode (precipitation mode).

by what is perturbed and at what scale. For example, T1 has T_s at 1-km spacing and a 1-km atmosphere grid, while TS1 has 1-km grids for T_s and soil moisture perturbations and the atmosphere. When the surface and atmosphere grid spacing differ, the suffix ''mix'' is used. Additional letters indicate the presence or absence of the Knievel et al. (2007) filter and the simulation depth. Thus, TSmix1_0.33NFs has 1-km soil moisture and T_s perturbations and 0.33-km atmosphere grid spacing, no Knievel filter (NF) and a shallow (*s*) domain.

TABLE 4. Criterion $-z_i/L$ for convective-roll occurrence from model and observations at 1830 UTC.

Date	Rolls?	$-z_i/L^*$ observed (aircraft u_*) (m)	$-z_i/L^*$ observed (surface u_*) (m)	$-L^{**}$ model ($z_0 = 0.12$ m) (m)	$-L^{**}$ model ($z_0 = 0.02$ m) (m)**	z_i mode1 (m)	$-z_i/L^{**}$ model ($z_0 = 0.12$ m)	$-z_i/L^{**}$ model ($z_0 = 0.02$ m)
30 May 2002	No	43	76	16	7	1350	81	199
17 Jun 2002	Yes	11	24	87	35	1325	15	38
20 Jun 2002	Yes	27	49	32	13	1340	41	100
22 Jun 2002	Yes	6	12.6	144	55	1750	12	32

* z_i data from Table 1, L calculated from aircraft and surface fluxes processed as described in Strassberg et al. (2008).

** Using H, LE, observed T, P, and Q, Monin–Obukhov similarity to find $-L$. $z_0 = 0.12$ m is grassland value for MODIS land use table; $z_0 = 0.02$ m is close to the observed value.

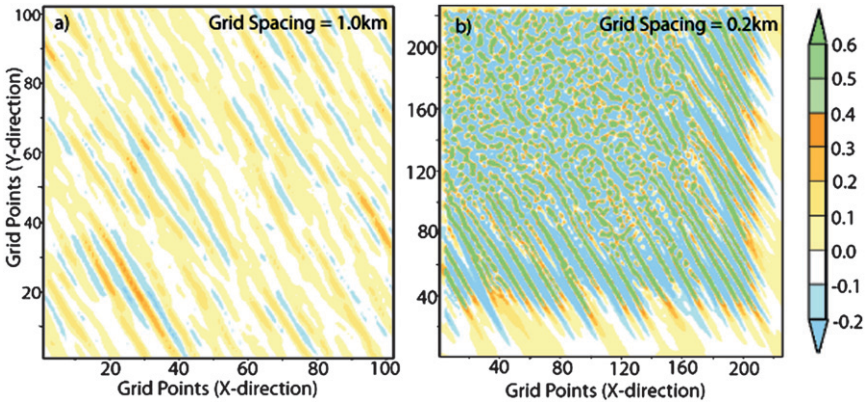

FIG. 7. Effect of grid spacing on CBL structure, as shown by mid-CBL (level 5, ~500 m) vertical-velocity fields (m s^{-1}) at 1800 UTC (a) from TS1 (T_s and volumetric soil moisture perturbations at atmospheric grid points, spaced 1 km apart) and (b) from TSmix1_0.2NFs (T_s and volumetric soil moisture perturbations on 1-km grid, atmosphere on 0.2-km grid).

Roll wavelengths in Table 2 were determined by manually counting vertical-velocity maxima or minima in the x direction (east–west) for direct comparison to grid spacing. However, roll aspect ratios (roll spacing divided by z_i) were calculated using the true roll spacing (measured normal to the roll axis). In nested runs, rolls were counted and convective type evaluated far enough downstream of the outer grid to mitigate boundary effects. For example, the convection in Fig. 7b would be considered ''cellular.''

The data in Table 2 suggest four general tendencies.

First, roll spacing in the x direction decreased with smaller grid size. For 22 June, the 1-km run (control) had rolls ranging from 2 km ($2\Delta x$) to ~4.5 km across, while the 333-m runs (HiResE and HiResW) typically had 2-km rolls. For the idealized runs, the reduction of roll size in the x-direction with smaller grids was clearly associated with the Knievel filter, which damps out perturbations smaller than $6\Delta x$ (6.7 km for TS1 versus 3.5 km for TS0.5). As in the case of 22 June, this trend was also evident without the filter (4.0, 2.4, and 1.8 km for TS1NF, TS0.5NFs, and TSmix1_0.33NFs, respectively). At the smallest atmosphere grid spacing with rolls (TSmix1_0.33NFs), their aspect ratio was 1.4, smaller than the expected land value (~2–3 or slightly greater). There also appear to be secondary effects related to domain top and the presence or absence of nesting. As expected, deactivating the Knievel filter led to smaller-scale rolls (6.7 km for TS1 versus 4.0 km for TS1NF).

Second, reducing the grid size led to more irregular convection. From the table, the two idealized runs with 200-m atmosphere grid spacing (T1mix1_0.2NFs and TS1mix1_0.2NFs) are dominated by cellular convection, rather than rolls; and the high-resolution 22 June runs had a mix of rolls and more three-dimensional structure in the 333-m grid inner domains. This tendency is illustrated by the change in structure between the 1800 UTC mid-CBL vertical-velocity fields for the idealized runs shown in Figs. 7 and 8, for a 1-km grid (TS1 in Fig. 7a, TS1NF in Fig. 8a) versus a 200-m atmosphere grid (TSmix1_0.2NFs in Fig. 7b). The behavior for TSmix1_0.2NFs was not changed significantly when we removed the Smagorinsky diffusion (not shown in Table 2). Trier et al. (2004) similarly found that convection changed from linear to more cellular when their grid spacing was changed from 3.3 to 1.1 km in their ARW-WRF simulations using the Mellor–Yamada–Janjic (MYJ) PBL scheme.

Third, CBL convective structures with T_s perturbations alone developed later than CBL convection with both T_s and soil moisture perturbations, or failed to develop at all, leaving the YSU PBL scheme to do the vertical transport. This is illustrated by the 1-km simulations with and without soil moisture perturbations in Fig. 8, which at 1800 UTC show well-developed rolls for TS1NF but only infinitesimal resolved motions at for T1NF. The onset time for resolved convection in the temperature-perturbation runs is scale dependent. Of the runs at 1, 2, 4, and 10 km (T1NF, T1, T2, T4, T10), temperature perturbations generated CBL convection only for the 1-km unfiltered run (T1NF), which began to form roll-like convection by 2100 UTC (Fig. 8d). For the 200-m atmosphere grid (T1mix1_0.2NFs), convection formed earlier, but was cellular. The increase in convection growth rate with decreasing horizontal scale is consistent with the results of Weisman et al. (1997).

Fourth, CBL rolls tended to grow with time along with the CBL depth (21-UTC roll size under ''remarks'' in Table 2), indicating ARW-WRF was able to follow this behavior at all resolutions for which rolls were captured.

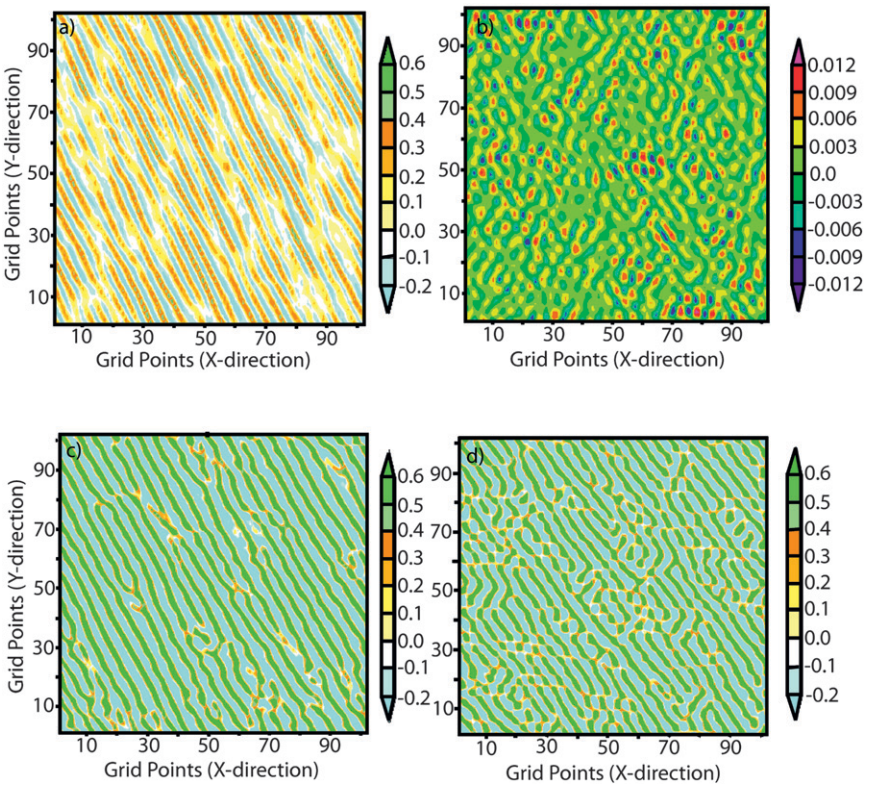

FIG. 8. Effect of volumetric soil moisture perturbations on CBL structure, as shown by mid-CBL (level 5, ~500 m) vertical velocity (m s^{-1}), for runs with no Knievel filter, at (top) 1800 and (bottom) 2100 UTC. (left) TS1NF (T_s and soil moisture perturbations at 1-km atmosphere grid spacing). (right) T1NF (like TS1NF but without soil moisture perturbations).

c. *Mesoscale motions*

LeMone et al. (2002) documented ~60-km circulations on 10 May 1997 linked to the Walnut River Watershed terrain. The repeatable along-track Θ_v differences through the mixed layer (Table 3) suggest the possibility of mesoscale circulations in IHOP_2002 as well. To estimate the time required to form a mesoscale circulation, we start with the idealized circulation equation for a sea breeze (Holton 1972), modified by (i) substituting the hydrostatic equation integrated from the surface to z_i assuming $T_v \approx \text{const} \approx \langle\Theta_v\rangle$ for the layer p_0 to p_{zi}, (ii) assuming that $\Delta\langle T_v\rangle \approx \Delta\langle\Theta_v\rangle$, and (iii) assuming that $z_i \ll \ell$, the length of the flight track:

$$\frac{du_\ell}{dt} \approx \frac{\Delta u_\ell}{\Delta t_{\Delta u_\ell}} \approx \frac{R}{2}\frac{\Delta\langle T_v\rangle}{(z_i+\ell)}\ln\frac{p_0}{p_{zi}} \approx \frac{4.9z_i}{\langle\Theta_v\rangle}\frac{\Delta\langle\Theta_v\rangle}{\ell}, \tag{4}$$

where u_ℓ is the component of the low-level wind along the ℓ direction, R is the gas constant, and p_0 and p_{zi} are the air pressure at the bottom and top of the CBL, respectively. Surface friction and Coriolis acceleration are neglected,[5] as well as interaction with turbulent eddies. The time $t_{\Delta u_\ell}$ along the air trajectory required for the wind to change by Δu_ℓ is thus

$$\Delta t_{\Delta u_\ell} \approx \Delta u_\ell\left(\frac{4.9z_i}{\langle\Theta_v\rangle}\frac{\Delta\langle\Theta_v\rangle}{\ell}\right)^{-1}, \tag{5}$$

where $\ell = 45.65$ km. Taking Δu_ℓ as 1 m s^{-1}, and values of $\Delta\langle\Theta_v\rangle$ and z_i from Table 3, $t_{\Delta u_\ell}$ varies from 1.4 h on 30 May to 3.1 h on 22 June, suggesting mesoscale circulations form most easily on 30 May. Multiplying by the along-trajectory wind (assumed equal to the measured values in Table 3), the corresponding along-trajectory

[5] Accounting for the retarding effects of friction would increase the time required to generate a circulation in (5). However, as pointed out in Holton and elsewhere, the frictional force increases as the square of the velocity. We neglect friction and Coriolis accelerations since our arguments are qualitative and we allow u_ℓ to increase to only 1 m s^{-1}. For more intense circulations, such as those considered in Miao and Geerts (2007) and Souza et al. (2000) or in considering how a steady state is reached, these effects are important.

distance $D_{\Delta u_t}$ required with $\Delta\langle\Theta_v\rangle$ values from the table ranges from 19 km for 30 May to 107 km for 22 June.

Given the rarity of direct observations of CBL mesoscale circulations, it is important to consider the conditions under which they can be observed. Once they are set up, mesoscale circulations should evolve slowly if they are to be observed using aircraft or even radar wind profilers. Under what conditions does this occur? A rapid dynamic response like that for 30 May will weaken the $\langle\Theta_v\rangle$ gradient and lead to a weaker or unsteady mesoscale circulation, unless the horizontal change of vertical flux divergence along the wind is sufficient to maintain the gradient against horizontal advection. Consider an air parcel in a two-dimensional circulation moving from point A on the cool side, with surface flux $\overline{w\theta_{v,0}}$ and virtual potential temperature $\langle\Theta_v\rangle$, to point B on the warm side, with flux $(1+f)\overline{w\theta_{v,0}}$ and virtual potential temperature $\langle\Theta_v\rangle + \Delta\langle\Theta_v\rangle$. We assume that the circulations are truly mesoscale, with the distance between A and B much greater than z_i, the scale of CBL large eddies; since the two scales would strongly interact otherwise.

At point M halfway between A and B, the surface buoyancy flux is halfway between point A and point B, namely $(1+0.5f)\overline{w\theta_{v,0}}$; which from (1), implies a vertical flux divergence warming within the CBL equal to $1.2(1+0.5f)\overline{w\theta_{v,0}}/z_i$. For $\langle\Theta_v\rangle_M$ at M to warm at the same rate as at point A, which from (1), is $1.2\overline{w\theta_{v,0}}/z_i$, advection $u_n(\partial\langle\Theta_v\rangle/\partial x) \approx u_n(\Delta\langle\Theta_v\rangle/D_{\rm AB})$, where $D_{\rm AB}$ is the distance between A and B, has to be just enough to offset the "extra warming." That is,

$$\frac{1.2(1+0.5f)\overline{w\theta_{v,0}}}{z_i} - u_n\frac{\Delta\langle\Theta_v\rangle}{D_{\rm AB}} \approx \frac{1.2\overline{w\theta_{v,0}}}{z_i}, \qquad (6)$$

where u_n is the wind from A to B at M, and z_i is assumed constant horizontally. Solving (6)

$$\frac{u_n\langle\Delta\Theta_v\rangle}{D_{\rm AB}} \approx \frac{0.6f\overline{w\theta_{v,0}}}{z_i}, \quad \text{or}$$

$$D_{\rm AB} \approx u_n\langle\Delta\Theta_v\rangle\frac{z_i}{0.6f\overline{w\theta_{v,0}}}. \qquad (7)$$

Taking $u_n = 1$ m s^{-1}, $z_i = 1000$ m, and $\overline{w\theta_{v,0}} = 0.1$ K m s^{-1}, the distance $D_{\rm AB}$ corresponding to the steady state is $16.7\Delta\langle\Theta_v\rangle/f$ km. These idealized calculations with f = 0.2 suggest $D_{\rm AB} = 50$ km (roughly flight-track scale) for 30 May ($\Delta\langle\Theta_v\rangle = 0.6$ K). For mesoscale circulations of this size, warming by vertical flux divergence just offsets cooling from horizontal advection and the Θ_v gradient can be maintained.

These arguments about maintenance of a constant $\langle\Theta_v\rangle$ gradient of course apply only under the assumptions that $\overline{w\theta_{v,zi}} = -0.2\overline{w\theta_{v,0}}$, z_i is constant horizontally, friction and Coriolis effects are negligible, and turbulence does not interact with the circulations. Some authors have simulated unsteady mesoscale circulations (Letzel and Raasch 2003), which Kang and Davis (2008) attribute to larger-amplitude horizontal $\overline{w\theta_{v,0}}$ variations.

Kang (2009) suggests that mesoscale circulations become unsteady because of interaction with turbulent eddies when their circulation velocity reaches $V_C \approx u_t(\lambda_C/2\lambda_t)^{0.5}$, where λ_C is the wavelength of the circulation (twice our $D_{\rm AB}$), and u_t and λ_t are the characteristic velocity and scale, respectively, of the turbulent (our kilometer scale) eddies. For typical values of $\lambda_t \approx 1.5z_i$, $z_i \approx 1000$ m, $u_t \approx 1$ m s^{-1}, and $\lambda_C = 100$ km, $V_C = 5.8$ m s^{-1}, much greater the 1 m s^{-1} used to estimate the wavelength for steady state. For the modeled horizontal variability in $\overline{w\theta_{v,0}}$ along the eastern track on 30 May (40 W m^{-2}, Fig. 4 in Part I), the mesoscale eddies modeled by Kang (2009) simply grow linearly at these scales for several hours, making them straightforward to observe. Smaller wavelengths (or larger horizontal flux variations) lead to oscillations developing more rapidly. Nevertheless, *in an average sense*, surface-heterogeneity-driven smaller-scale circulations are produced in LESs down to kilometer scale by Avissar and Schmidt (1998), Patton et al. (2005), and many others; and Grossman et al. (2005) observed averaged circulations of 10-km scale.

d. Observational evidence of mesoscale circulations

Figure 9 shows that estimates of the along-track divergence of the along-track wind component are consistent with the development of along-track mesoscale circulations in the CBL on 30 May (and possibly 17 June), with convergence (divergence) in the lower CBL and divergence (convergence) in the upper CBL. The divergence pattern on 22 June indicates subsidence. The 20 June divergences are less than the standard error.

We do not expect exact correspondence between the divergence-derived mean vertical velocities[6] (W) from the ABLE radar wind profiler triangle in Fig. 10 and the aircraft-derived divergences in Fig. 9; since the latter are only for the wind component parallel to the flight track, and the two measurements are displaced horizontally (Fig. 1). However, the two sets of measurements together reveal some interesting patterns. Figures 9 and 10 both indicate strong subsidence on 22 June. There is evidence for circulations largely confined to the CBL on

[6] The unusually large negative values are related to the ground rising northward by about 200 m within the profiler triangle in Fig. 1. To obtain a true vertical wind relative to the center of the earth, a correction related to the wind vector and the gradient in terrain along that vector would be needed.

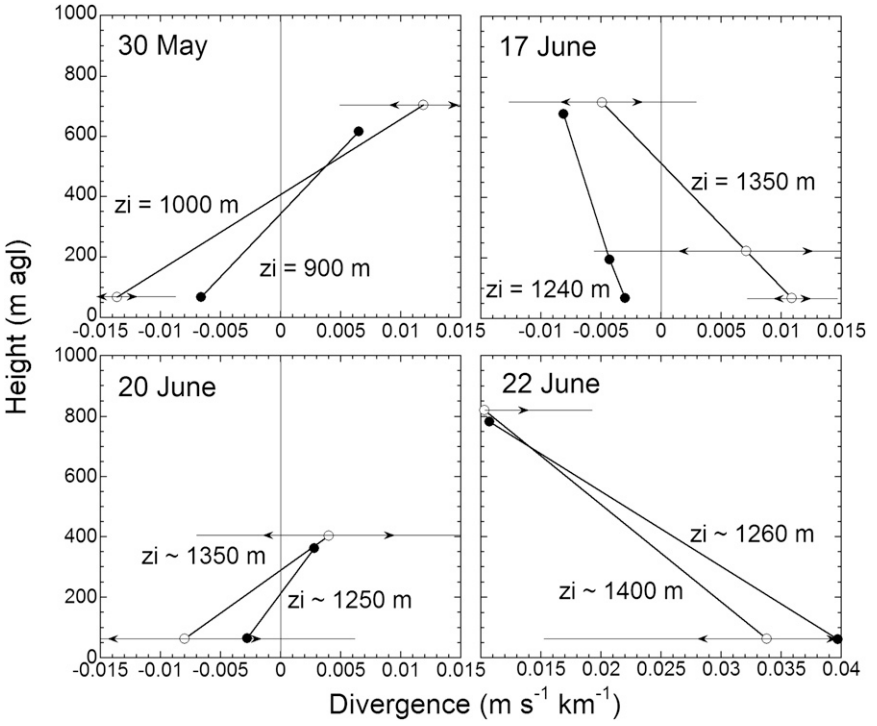

FIG. 9. Aircraft-based profiles of along-track divergence of the along-track wind component, for the four IHOP_2002 days. Solid circles: profiles at 1830 UTC; open circles: profiles at 1930 UTC. Error bars applying to both profiles plotted on 1930 UTC values: lines show standard deviation σ about best-fit straight line to time series of divergence values; arrows show corresponding standard error $\sigma/\sqrt{n}$, where n is the number of divergence estimates. For comparison, uncertainty estimates from Eq. (A11) of Lenschow et al. (1980) for the low-level legs on the 4 days in chronological order are 0.0075, 0.010, 0.011, and 0.009 m s^{-1} km^{-1}.

30 May, with convergence in the lower CBL and divergence in the upper CBL in Fig. 9 and *W* extrema within the CBL at 1600 UTC and possibly 2000 UTC in Fig. 10, but not at other times. On 20 June at 1600 UTC, there is subsidence that reaches a maximum at around 1300 m AGL (almost $2z_i$), suggesting a circulation that extends above the CBL, but aircraft-based convergence is smaller than the expected error and available only below 450 m AGL. On 17 June, the *W* extremum at 2000 UTC is within the CBL in Fig. 10 and corresponds roughly to the top of the divergence layer at 1930 UTC in Fig. 9; but there are *W* extrema above the CBL at 1800 and 1900 UTC. *We interpret these figures as suggestive of mesoscale circulations on 30 May and possibly 17 June, possible mesoscale features centered above the CBL on 20 June, and no detectable mesoscale circulations in the CBL on 22 June.*

To see whether the mesoscale features are replicated in ARW-WRF, we produced horizontal fields in domain d03 of temperature at ARW-WRF level 3 (about 300 m AGL) and the vertical velocity at ARW-WRF level 5 (about 500 m AGL) and applied a bidirectional 121-point box filter (11 km in each direction). The resulting plots appear in Figs. 11a and 11b. At scales of tens of kilometers, we see circulations based in the CBL on 30 May and circulations with maximum amplitude above the CBL on 20 June. Mesoscale structures on 22 June are overwhelmed by the rolls. On 17 June, there are some weak warm upwelling regions and cool downwelling regions in the CBL; but little mesoscale circulation evident in the cross section in Fig. 11a, with maxima and minima above the CBL at 1800 UTC, consistent with the ambiguous observations in Figs. 9 and 10. There is a large response to the Wichita urban heat island (Fig. 12) on 30 May (distance = 20 km in cross section, Fig. 11a), but only a small response on the remaining three days (Figs. 11a,b).

The circulations on 30 May appear to be examples of the classic ''inland sea breeze,'' as studied by Ogura and Chen (1977), Sun and Ogura (1979), Anthes (1984), Segal et al. (1988), Pielke et al. (1991), and many others, with upwelling (downwelling) areas correspond to warmer (cooler) air in the CBL (Fig. 11a). Indeed, Gorska et al. (2008) simulated mesoscale circulations using an LES with the lower boundary conditions idealized from HRLDAS

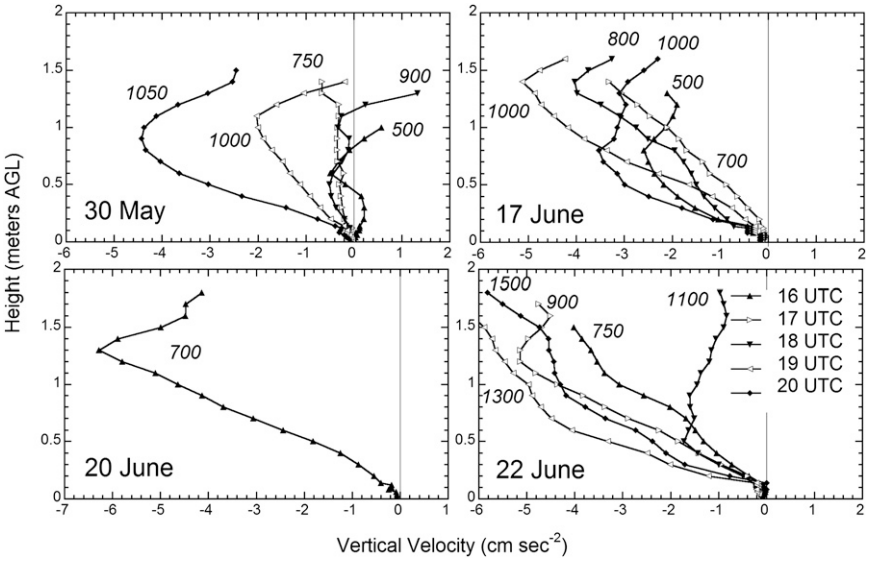

FIG. 10. ABLE radar-wind profiler triangle convergence-based estimates of mean vertical velocity W. The CBL depth in meters inferred from the radar wind profilers appears next to each profile. Values are likely too negative since terrain has not been taken into account, with bias increasing with wind speed.

output for 30 May for the eastern track region. The general subsidence over the profiler triangle corresponds roughly to observations (Fig. 10), but the pattern along the flight track is less clear. Exact correspondence is not expected given differences in the observed and modeled fluxes, discussed in Part I. From Fig. 8 in Part I, the modeled PBL top is around 850–830 hPa; thus, the 30 May cross section in Fig. 11a indicates maximum vertical velocities within the CBL, with the largest updraft–downdraft couplet associated with the Wichita urban heat island and its flux anomaly (Fig. 12). All of these features were preserved when this day was rerun using ARW-WRF version 3.0 with the Knievel filter. From the previous discussion, the upstream flux contrast results in strong temperature gradients (Fig. 11a; Table 3), which favor mesoscale circulations. Moreover, the temperature gradient, scale, and flux differences are roughly consistent with near steady state, a condition required for being well observed in a ~4-h aircraft mission.

While there are localized mesoscale circulations apparently driven by CBL temperature contrast (Fig. 11b, top), there are well-defined linear structures normal to the convective rolls across the region on 20 June (Figs. 5b and 11b) that appear unrelated to the CBL temperature. The vertical-velocity amplitudes in the 20 June cross section in Fig. 11b reach a maximum above the CBL, at about 700 mb. We speculate that the 700-mb extrema are associated with the northeast–southwest linear structures, and that both are due to gravity waves. As obvious from the figures, ARW-WRF replicates both the wavelength and the orientation. However, there is a mismatch in phase speed (14 m s^{-1} for ARW-WRF, nearly stationary in the observations), so this is speculation at this point.

It is interesting that even on 30 May, when mesoscale circulations were favored; they were not clearly related to the Walnut River Watershed, as was the case in LeMone et al. (2002). We believe that the explanation has to do with the association of vegetation type with elevation in the watershed. The circulation described in LeMone et al. (2002) was in early May, so that the warmth associated with the higher elevations (Walko et al. 1992; Krettenauer and Schumann 1992) was reinforced by higher surface air temperatures associated with dormant grasses there, with lower surface air temperatures above the rapidly growing winter wheat in the lower elevations. However, in the present summer case, the elevated terrain has its surface air temperature cooled due to evapotranspiration from the green grasses, while the lowlands have higher surface air temperatures due to dormant or harvested winter wheat.

5. Conclusions

Comparisons of satellite images and aircraft and surface observations centered along the IHOP_2002 eastern track to ARW-WRF–Noah modeling results on four fair-weather days with southerly winds and nearly clear skies, show that the model captures both the type of convective-scale structure (a few kilometers across) and

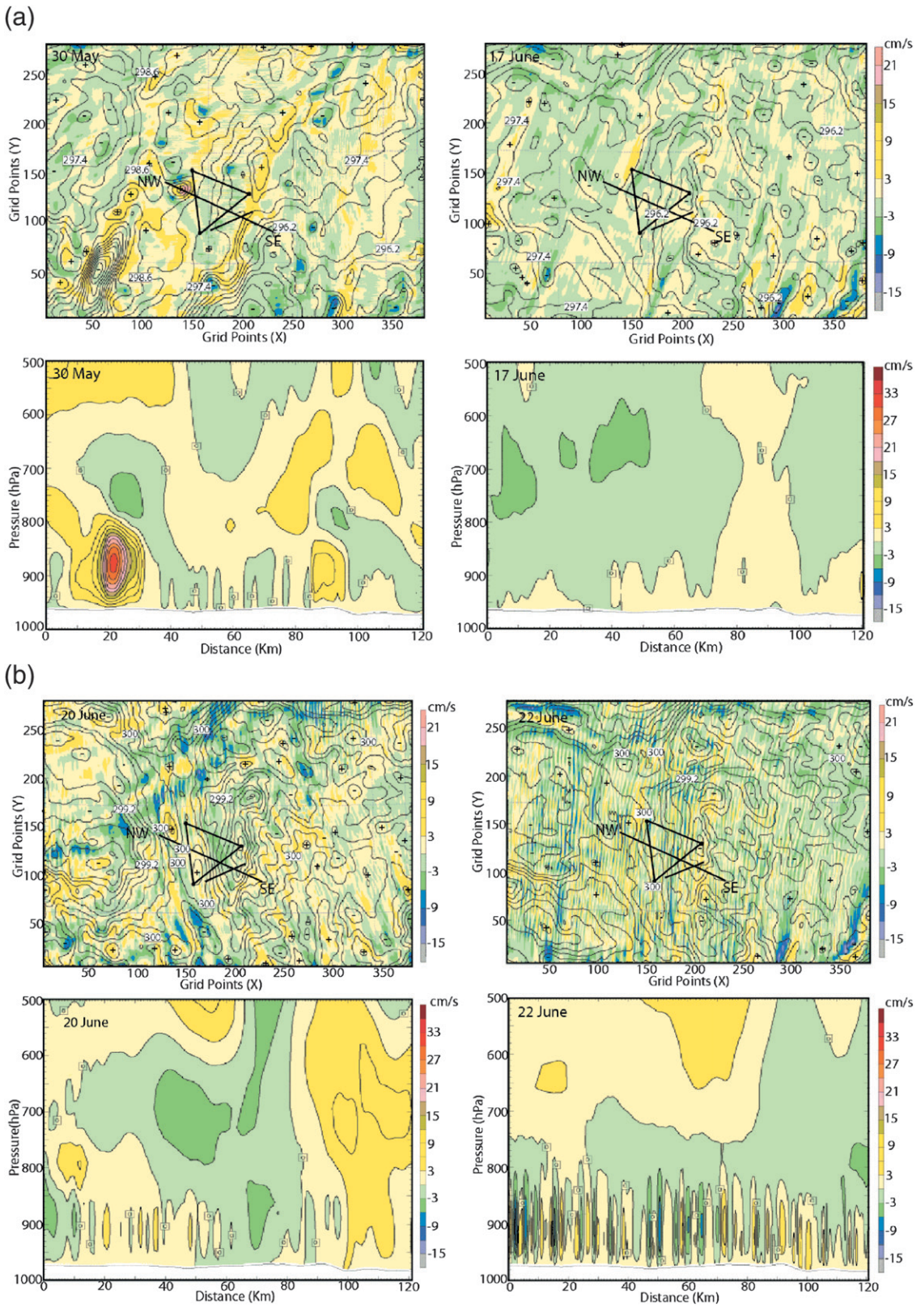
(a)
30 May
17 June
NW
SE
Grid Points (X)
Grid Points (Y)
Pressure (hPa)
Distance (Km)
cm/s
(b)
20 June
22 June
Pressure(hPa)

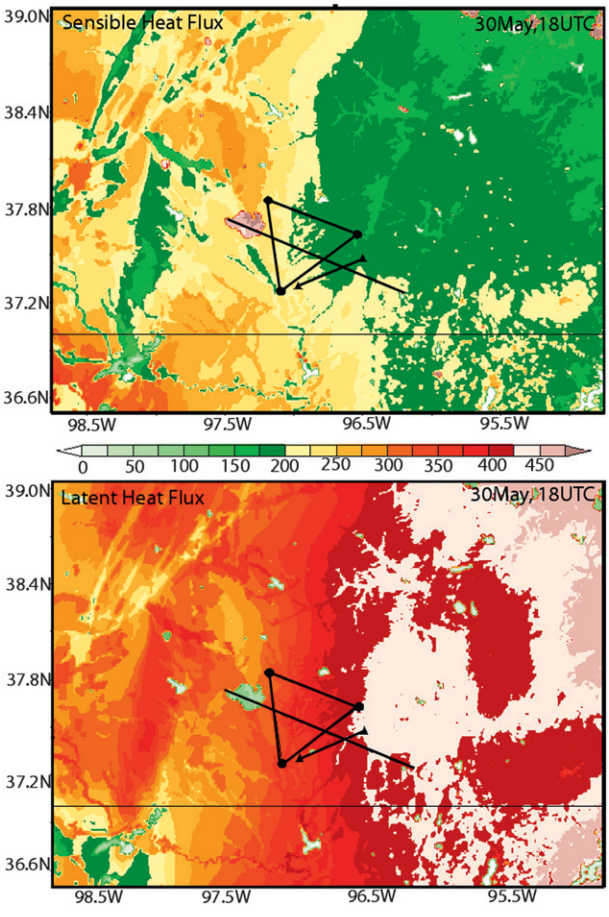

FIG. 12. Sensible and latent heat flux (W m^{-2}) for 1800 UTC 30 May 2002 for coupled ARW-WRF–Noah run. The area of largest sensible heat flux and smallest latent heat flux just to the west of the profiler triangle is associated with Wichita, KS, and suburbs (see land use/land cover in Figs. 1 and 2, bottom).

influence of surface heterogeneity on CBL mesoscale structure (tens of kilometers across) reasonably well. This is in spite of the model deficiencies discussed in Part I, namely significant overestimates of H and CBL depth and the model's inability to capture variability associated with vegetation because of the model input land-use land-cover table not including enough winter wheat pixels along and upwind the flight track.

While surprising given the probable mismatch of the PBL parameterization to the 1-km grid spacing, modeled two-dimensional CBL structures corresponded well to the cloud streets evident in the 17, 20, and 22 June satellite images, in terms of orientation, spacing, and on 2 out of 3 days, timing. Moreover, evidence from radar as well as satellite images shows that observed as well as modeled rolls occurred for the range of $-z_i/L < 25$ associated with roll occurrence by Weckwerth et al. (1999) and others. For both model and observations, the L values corresponded better to "regional" values of z_0 ($\approx$0.1 m), which implicitly account for larger roughness elements (e.g., trees and houses) as well as the vegetation (crops or grassland) specified. However, the "good" roll spacing and aspect ratios were fortuitous: sensitivity studies showed both were influenced by the grid spacing; and with grid spacing less than about 300 m, the rolls broke down into cells. While realistic model convective type is surprising, the change in model behavior at smaller grid sizes is not, given the combined effects of poor horizontal resolution, the potential for double counting created by resolved CBL motions in a PBL scheme designed for larger grid sizes, and the reduction in the aspect ratio of the grid boxes (Wyngaard et al. 1998; Wyngaard 2004).

On scales $\geq\sim$30 km, ARW-WRF again replicates the type of mesoscale structure expected from observations. Mesoscale circulations associated with CBL temperature differences are modeled on 30 May, the day for which they were most likely, given the large along-track Θ_v difference and light winds. A sensitivity run using ARW-WRF 3.0 and the Knievel filter produced nearly identical mesoscale structure. On this day, both along-track divergence of the along-track aircraft wind and some radar wind profiler vertical velocity estimates are consistent with CBL circulations, with extrema within the CBL. Idealized trajectory analysis based on model results suggested there was enough horizontal contrast on a large enough scale to create the observed along-track Θ_v difference. Idealized analysis of the circulation and effects of horizontal advection suggested that mesoscale circulations could develop fairly rapidly on this day, and be sufficiently steady state to be observable using aircraft, for wavelengths of the order of 100 km.

←

FIG. 11. (a) ARW-WRF mesoscale vertical-velocity (shading, color bars to right) and temperature fields (contours, top frames only) for (left) 1800 UTC 30 May and (right) 1800 UTC 17 Jun 2002. (top) Maps of temperature at level 3 ($\sim$300 m, AGL, contour interval 0.2 K, maxima and minima denoted by "+" and "−") and vertical velocity at level 5 ($\sim$500 m AGL); (bottom) vertical cross section of vertical velocity along the northwest–southeast line on the maps. Data filtered using a 121-point (11 km × 11 km) horizontal box filter. The northwest–southeast line extends from 37.73°N, 97.5°W to 37.28°N, 96.25°W. Map grid points are 1 km apart. Model CBL depth at around 50-80 km along cross section: $\sim$830–850 hPa for 30 May, and $\sim$830 hPa for 17 June. (b) As in (a), but for 1800 UTC 20 Jun and 1800 UTC 22 Jun 2002. Model CBL depth at around 50–80 km along cross section: $\sim$830 hPa for 20 June, and $\sim$800 hPa for 22 June.

There is mesoscale variability in both the observations and the model on 20 June, with patches of surface-driven circulations, but, more interestingly, intensity changes in the north-northwest–south-southeast cloud streets marked by northeast–southwest bands of nearly-clear skies and enhanced cloudiness. This modulation is not associated with temperature changes in the CBL and the amplitude of the vertical-velocity variation peaks above the CBL, suggesting gravity waves. A mismatch between observed and modeled phase speeds indicates more work is needed to confirm this hypothesis. No mesoscale CBL variation is evident either in the satellite image or in the ARW-WRF simulations for 22 June, the day with uniform observed subsidence, the least horizontal contrast, and the strongest winds. None of the mesoscale circulations were clearly linked to the topography sampled by the aircraft and profilers, as in the case described in LeMone et al. (2002) for the same region, perhaps because the thermal effects of land cover and elevation were in opposite directions during IHOP_2002, while they reinforced one another in the former case.

In this paper, we were careful to compare the type rather than the details of CBL and lower-tropospheric structure on scales from kilometers to tens of kilometers, because either the model or the data were not adequate for a closer comparison. The major model shortcomings—the inability to represent the impact of the dormant/harvested winter wheat in the mixed grass-winter wheat regions, and the overestimate of surface sensible heat flux—can be dealt with in a straightforward way. Indeed, a new formulation for C in the Noah LSM based on Chen and Zhang (2009) should improve modeled surface fluxes. The impact on this change on ARW-WRF is currently being tested (S. Trier 2009, personal communication). To deal with observational shortcomings, we will simulate the well-documented mesoscale circulations observed during the Cooperative Atmosphere-Surface Exchange Study-97 (CASES-97) and documented in LeMone et al. (2002). Like the present work, however, the future work will require finer grid spacing than optimum for present ARW-WRF PBL schemes.

Acknowledgments. This work would not have been possible without the commitment, enthusiasm, and expertise of the Wyoming King Air aircrew, the staff maintaining the Wyoming Cloud Radar, the National Center for Atmospheric Research (NCAR) staff maintaining the surface flux instruments, and the students taking the manual observations at the flux sites. We gratefully acknowledge the four reviewers whose thorough reviews improved the manuscript and Stan Trier of NCAR for supplying filtering software for the ARW-WRF data, and for reviewing the manuscript, as well as discussions with George Bryan and Chin-Hoh Moeng in designing and interpreting our sensitivity studies. The NCAR portion of this research was supported by USWRP Grant NSF 01, the NCAR Water Cycle Initiative, and NASA-THP (Grant NNG06GH17G) and NOAA/JCSDA (Grant NA06NES4400013), as well as NCAR base funding. RLG's participation in IHOP_2002 was supported by NSF Grant ATM-0296159. RC's work was supported by the U.S. Department of Energy, Office of Biological and Environmental Research, under Contract W-31-109-Eng-38.

REFERENCES

Angevine, W. M., 1997: Errors in mean vertical velocities measured by boundary layer wind profilers. *J. Atmos. Oceanic Technol.,* **14,** 565–569.

Anthes, R. A., 1984: Enhancement of convective precipitation by mesoscale variations in vegetative covering in semiarid regions. *J. Climate Appl. Meteor.,* **23,** 541–554.

Avissar, R., and T. Schmidt, 1998: An evaluation of the scale at which ground surface heat flux patchiness affects the convective boundary layer using large-eddy simulations. *J. Atmos. Sci.,* **55,** 2666–2689.

Baidya Roy, S., and R. Avissar, 2000: Scales of response of the convective boundary layer to land-surface heterogeneity. *Geophys. Res. Lett.,* **27,** 533–536.

——, C. P. Weaver, D. S. Nolan, and R. Avissar, 2003: A preferred scale for landscape forced mesoscale circulations? *J. Geophys. Res.,* **108,** 8854, doi:10.1029/2002JD003097.

Balaji, V., J.-L. Redelsperger, and G. P. Klaasen, 1993: Mechanisms for the mesoscale organization of tropical cloud clusters in GATE Phase III. Part I: Shallow cloud bands. *J. Atmos. Sci.,* **50,** 3571–3589.

Chen, F., and R. Avissar, 1994: The impact of land-surface wetness heterogeneity on mesoscale heat fluxes. *J. Appl. Meteor.,* **33,** 1323–1340.

——, and J. Dudhia, 2001: Coupling an advanced land surface hydrology model with the Penn State–NCAR MM5 modeling system. Part I: Model implementation and sensitivity. *Mon. Wea. Rev.,* **129,** 569–585.

——, and Y. Zhang, 2009: On the coupling strength between the land surface and the atmosphere. *Geophys. Res. Lett.,* **36,** L10404, doi:10.1029/2009GL037980.

——, and Coauthors, 2007: Description and evaluation of the characteristics of the NCAR high-resolution land data assimilation system. *J. Appl. Meteor. Climatol.,* **46,** 694–713.

Clark, T. L., T. Hauf, and J. P. Kuettner, 1986: Convectively forced internal gravity waves: Results from two-dimensional experiments. *Quart. J. Roy. Meteor. Soc.,* **112,** 899–926.

Conzemius, R. J., and E. Fedorovich, 2006: Dynamics of sheared convective boundary layer entrainment. Part I: Methodological background and large-eddy simulations. *J. Atmos. Sci.,* **63,** 1151–1178.

——, and ——, 2008: A case study of convective boundary layer development during IHOP_2002: Numerical simulations compared to observations. *Mon. Wea. Rev.,* **136,** 2305–2320.

Coulter, R. L., and D. Holdridge, 1998: A procedure for the automatic estimation of mixed layer height. *Proc. Eighth Atmospheric Radiation Measurement (ARM) Program Science*

Team Meeting, Tucson, AZ, Dept. of Energy Office of Energy Research, 177–180.

Davis, C., and Coauthors, 2008: Prediction of landfalling hurricanes with the advanced hurricane WRF model. *Mon. Wea. Rev.,* **136,** 1990–2005.

Deardorff, J. W., 1972: Numerical investigation of neutral and unstable planetary boundary layers. *J. Atmos. Sci.,* **29,** 91–115.

Desai, A. R., K. J. Davis, C. J. Senff, S. Ismail, E. V. Browell, D. R. Stauffer, and B. P. Reen, 2006: A case study on the effects of heterogeneous soil moisture on mesoscale boundary-layer structure in the southern Great Plains, USA. Part I: Simple prognostic model. *Bound.-Layer Meteor.,* **119,** 195–238.

Ek, M. B., K. E. Mitchell, Y. Lin, E. Rogers, P. Grummann, V. Koren, G. Gayno, and J. D. Tarpley, 2003: Implementation of Noah land surface model advances in the National Centers for Environmental Prediction operational mesoscale Eta model. *J. Geophys. Res.,* **108,** 8851, doi:10.1029/2002JD003296.

Gorska, M., J. Vila-Guerau de Arellano, M. A. LeMone, and C. C. van Heerwaarden, 2008: Mean and flux horizontal variability of virtual potential temperature, moisture, and carbon dioxide: Aircraft observations and LES study. *Mon. Wea. Rev.,* **136,** 4435–4451.

Grossman, R. L., D. Yates, M. A. LeMone, M. L. Wesely, and J. Song, 2005: Observed effects of horizontal radiative surface temperature variations on the atmosphere over a Midwest watershed during CASES 97. *J. Geophys. Res.,* **110,** D06117, doi:10.1029/2004JD004542.

Holton, J. R., 1972: *An Introduction to Dynamic Meteorology*. Academic Press, 319 pp.

Hong, S.-Y., Y. Noh, and J. Dudhia, 2006: A new vertical diffusion package with an explicit treatment of entrainment processes. *Mon. Wea. Rev.,* **134,** 2318–2341.

Kang, S., 2009: Temporal oscillations in the convective boundary layer forced by mesoscale surface heat-flux variations. *Bound.-Layer Meteor.,* **132,** 59–81, doi:10.1007/s10546-009-9391-5.

——, and K. J. Davis, 2008: The effects of mesoscale surface heterogeneity on the fair-weather convective atmospheric boundary layer. *J. Atmos. Sci.,* **65,** 3197–3213.

——, ——, and M. A. LeMone, 2007: Observations of the ABL structures over a heterogeneous land surface during IHOP_2002. *J. Hydrometeor.,* **8,** 221–244.

Klazura, G., and Coauthors, 2006: Atmospheric boundary layer measurements in south-central Kansas, 1997–2004. *Bull. Amer. Meteor. Soc.,* **87,** 1319–1324.

Knievel, J. C., G. H. Bryan, and J. P. Hacker, 2007: Explicit numerical diffusion in the WRF model. *Mon. Wea. Rev.,* **135,** 3808–3824.

Krettenauer, K., and U. Schumann, 1992: Numerical simulation of turbulent convection over wavy terrain. *J. Fluid Mech.,* **237,** 261–299.

Lafore, J.-P., and Coauthors, 1998: The Meso-NH atmospheric simulation system. Part I: Adiabatic formulation and control simulations. *Ann. Geophys.,* **16,** 90–109.

LeMone, M. A., 1973: The structure and dynamics of horizontal roll vortices in the planetary boundary layer. *J. Atmos. Sci.,* **30,** 1077–1091.

——, and Coauthors, 2002: CASES-97: Late-morning warming and moistening of the convective boundary layer over the Walnut River watershed. *Bound.-Layer Meteor.,* **104,** 1–52.

——, and Coauthors, 2007: NCAR/CU surface, soil, and vegetation observations during the International H_2O Project 2002 field campaign. *Bull. Amer. Meteor. Soc.,* **88,** 65–81.

——, F. Chen, M. Tewari, J. Dudhia, B. Geerts, Q. Miao, R. L. Coulter, and R. L. Grossman, 2010: Simulating the IHOP_2002 fair-weather CBL with the WRF-ARW–Noah modeling system. Part I: Surface fluxes and CBL structure and evolution along the eastern track. *Mon. Wea. Rev.,* **138,** 722–744.

Lenschow, D. H., J. C. Wyngaard, and W. T. Pennell, 1980: Mean-field and second-moment budgets in a baroclinic, convective boundary layer. *J. Atmos. Sci.,* **37,** 1313–1326.

Letzel, M. O., and S. Raasch, 2003: Large eddy simulation of thermally induced oscillations in the convective boundary layer. *J. Atmos. Sci.,* **60,** 2328–2341.

Lothon, M., F. Couvreux, S. Donier, F. Guichard, P. Lacarrere, D. H. Lenschow, J. Noilhan, and F. Said, 2007: Impact of coherent eddies on airborne measurements of vertical turbulent fluxes. *Bound.-Layer Meteor.,* **124,** 425–447, doi:10.1007/s10546-007-9182-9.

Mahrt, L., J. Sun, D. Vickers, J. I. MacPherson, J. R. Pederson, and R. L. Desjardins, 1994: Observations of fluxes and inland breezes over a heterogeneous surface. *J. Atmos. Sci.,* **51,** 2484–2499.

Miao, Q., and B. Geerts, 2007: Finescale vertical structure and dynamics of some dryline boundaries observed in IHOP. *Mon. Wea. Rev.,* **135,** 4161–4184.

Miao, S., and F. Chen, 2008: Formation of horizontal convective rolls in urban areas. *Atmos. Res.,* **89,** 298–304, doi:10.1016/j.atmosres.2008.02.013.

Moeng, C.-H., and P. P. Sullivan, 1994: A comparison of shear- and buoyancy-driven planetary boundary layer flows. *J. Atmos. Sci.,* **51,** 999–1022.

Ogura, Y., and Y. Chen, 1977: A life history of an intense mesoscale convective system in Oklahoma. *J. Atmos. Sci.,* **34,** 1458–1476.

Patton, E. G., P. P. Sullivan, and C.-H. Moeng, 2005: The influence of idealized heterogeneity on wet and dry planetary boundary layers coupled to the land surface. *J. Atmos. Sci.,* **62,** 2078–2097.

Pielke, R. A., G. Dalu, J. Snook, T. Lee, and T. Kittell, 1991: Nonlinear influence of mesoscale land use on weather and climate. *J. Climate,* **4,** 1053–1069.

Reen, B. P., D. R. Stauffer, K. J. Davis, and A. R. Desai, 2006: A case study on the effects of heterogeneous soil moisture on mesoscale boundary-layer structure in the southern Great Plains, USA. Part II: Mesoscale modelling. *Bound.-Layer Meteor.,* **120,** 275–314.

Segal, M., R. Avissar, M. McCumber, and R. Pielke, 1988: Evaluation of vegetation effects on the generation and modification of mesoscale circulations. *J. Atmos. Sci.,* **45,** 2268–2292.

Skamarock, W. C., 2004: Evaluating mesoscale NWP models using kinetic energy spectra. *Mon. Wea. Rev.,* **132,** 3019–3032.

——, J. B. Klemp, J. Dudhia, D. O. Gill, D. M. Barker, W. Wang, and J. G. Powers, 2005: A description of the Advanced Research WRF version 2. NCAR Tech. Note TN-468+STR, 88 pp. [Available from NCAR, P.O. Box 3000, Boulder, CO 80307.]

Souza, E. P., N. O. Renno, and M. A. F. Silva Dias, 2000: Convective circulations induced by surface heterogeneities. *J. Atmos. Sci.,* **57,** 2915–2922.

Strassberg, D., M. LeMone, T. Warner, and J. Alfieri, 2008: Comparison of observed 10-m wind speeds to those based on Monin–Obukhov similarity theory using IHOP_2002 aircraft and surface data. *Mon. Wea. Rev.,* **136,** 964–972.

Sun, W.-Y., and Y. Ogura, 1979: Boundary-layer forcing as a possible trigger to a squall-line formation. *J. Atmos. Sci.,* **36,** 235–254.

Taylor, C. M., D. J. Parker, and P. P. Harris, 2007: An observational case study of mesoscale atmospheric circulations induced by soil moisture. *Geophys. Res. Lett.,* **34,** L15801, doi:10.1029/2007GL030572.

Trier, S. B., F. Chen, and K. W. Manning, 2004: A study of convection initiation in a mesoscale model using high-resolution land-surface initial conditions. *Mon. Wea. Rev.,* **132,** 2954–2976.

Walko, R. L., W. R. Cotton, and R. A. Pielke Sr., 1992: Large-eddy simulations of the effects of hilly terrain on the convective boundary layer. *Bound.-Layer Meteor.,* **58,** 133–150.

Weckwerth, T. M., T. W. Horst, and J. W. Wilson, 1999: An observational study of the evolution of horizontal convective rolls. *Mon. Wea. Rev.,* **127,** 2160–2179.

——, and Coauthors, 2004: An overview of the International H_2O Project (IHOP_2002) and some preliminary highlights. *Bull. Amer. Meteor. Soc.,* **85,** 253–277.

Weisman, M. L., W. C. Skamarock, and J. B. Klemp, 1997: The resolution dependence of explicitly modeled convective systems. *Mon. Wea. Rev.,* **125,** 527–548.

Wyngaard, J. C., 2004: Toward numerical modeling in the ''Terra Incognita.'' *J. Atmos. Sci.,* **61,** 1816–1826.

——, L. J. Peltier, and S. Khanna, 1998: LES in the surface layer: Surface fluxes, scaling, and SGS modeling. *J. Atmos. Sci.,* **55,** 1733–1754.

Young, G. S., D. A. R. Kristovich, M. R. Hjelmfelt, and R. C. Foster, 2002: Rolls, streets, waves, and more: A review of quasi-two-dimensional structures in the atmospheric boundary layer. *Bull. Amer. Meteor. Soc.,* **83,** 997–1001.